

PERIODICO di MINERALOGIA
established in 1930

*An International Journal of
MINERALOGY, CRYSTALLOGRAPHY, GEOCHEMISTRY,
ORE DEPOSITS, PETROLOGY, VOLCANOLOGY*
and applied topics on *Environment, Archeometry and Cultural Heritage*

Structural and spectroscopic characterization of anorthite synthesized from secondary raw materials

Alessandro Francesco Gualtieri^{1,*}, Giovanni B. Andreozzi², Carlotta Giacobbe¹,
Gigliola Lusvardi³ and Cecilia Viti⁴

¹Dipartimento di Scienze della Terra, University of Modena and Reggio Emilia, Italy

²Dipartimento di Scienze della Terra, Sapienza University of Rome, Italy

³Dipartimento di Chimica, University of Modena and Reggio Emilia, Italy

⁴Dipartimento di Scienze della Terra, University of Siena, Italy

*Corresponding author: alessandro.gualtieri@unimore.it

Abstract

Recycling of secondary raw materials is a priority of waste handling in the countries of the European community. A virtual secondary raw material of great importance is the product of the thermal transformation of cement – asbestos. This work illustrates the study of calcination products obtained starting from the product of the thermal transformation of cement-asbestos at 1200 °C, added to primary raw materials (kaolin, aluminum hydroxide) and boric acid as mineralizing agent. The calcination has been conducted at 1200 °C for 1 hour. The crystallization kinetics has been monitored using in situ high temperature X-ray powder diffraction. The microscopic characterization of the final product of calcination has been conducted with SEM and TEM imaging supported by X-ray microanalysis. The structure refinement was conducted on the powder sample using the Rietveld method. The results are compared with the spectroscopic characterization including Mössbauer and UV-Vis spectroscopies. The final product of the calcination is essentially anorthite (about 89 wt%) with minor spinel (11 wt%). All experimental data converge to support the hypothesis that the anorthite is stoichiometric, and the small amounts of iron detected (1.32 wt%) is Fe³⁺ hosted in the structure of spinel.

Key Words: Anorthite; synthesis; KRY·AS; Rietveld refinement; Fe-spinel.

Introduction

Plagioclase feldspars, a solid solution comprised within the end-members NaAlSi₃O₈ albite and

CaAl₂Si₂O₈ anorthite, are among the most abundant minerals at the Earth's crust. From geological point of view, plagioclase feldspars have a great potential for geobarometric and

geothermometric applications, even if it is well known that their diverse subsolidus behavior has challenged understanding (Angel, 1998). In addition, anorthite-bearing rocks (e.g., anorthosite) and synthetic anorthite offer a great variety of industrial applications (Wanvik, 2000). They can be used as raw materials for dry or wet mineral processing (aggregates, building materials, fillers, abrasives, extenders, and coatings) or for acid or alkaline leaching processes (extraction of Al, sizing, binders, catalysts, and others). In the latter chemical applications, it is primarily the high Al content of anorthite or anorthosites which makes them attractive for a variety of industrial uses. The Al content can be utilized in various processes and anorthosite can be leached with mineral acids in order to facilitate its liberation (Wanvik, 2000).

The structure of plagioclase feldspars consists of a three-dimensional framework of corner-linked tetrahedra that host Al and Si atoms (Figure 1). The complexity of feldspar structures arises in part from the interplay between (Al, Si)-ordering among these tetrahedra and displacive

distortions of the framework as a whole (Angel, 1998). At temperatures approaching the melting point, there is basically complete solid solution between (Al, Si)-disordered albite and anorthite, although space groups range from $C2/m$ to $I\bar{1}$ (Ribbe, 1983). There are only two possible completely ordered (Al, Si) distributions in plagioclases: $C\bar{1}$ low albite and both $P\bar{1}$ and $I\bar{1}$ anorthite. In spite of that, Angel et al. (1990) found that even the most ordered anorthite from Val Paseda may be as much as 8% disordered. Ghose et al. (1993) in their neutron refinement of $I\bar{1}$ anorthite concluded that Al/Si ordering is virtually complete, but other evidences in the literature have left the issue of a partial ordering in anorthite open (Carpenter, 1991; Phillips et al., 1992). In primitive anorthite, although the c axis is $\approx 14 \text{ \AA}$, Ca^{2+} provokes a dramatic collapse of the tetrahedral framework. This gives rise to the generation of a number of non equivalent sites and an avalanche of site nomenclature (Ribbe, 1983). Primitive anorthite inverts to apparent $I\bar{1}$ symmetry at $T_c \approx 240 \text{ }^\circ\text{C}$ (Ribbe, 1983). In body centered anorthite c is still $\approx 14 \text{ \AA}$. Ghose et al.

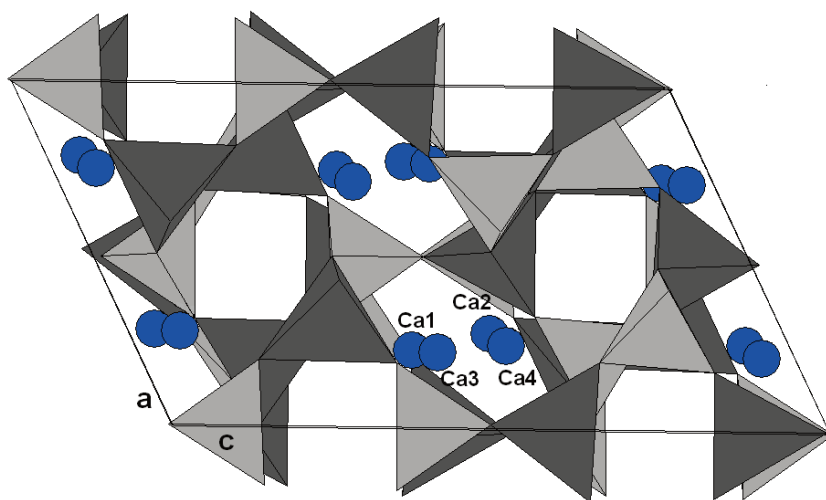


Figure 1. The structure of synthetic anorthite in the a-c plane. The light gray tetrahedra are centered by Si, the dark gray tetrahedra are centered by Al. Blue spheres represent the Ca atoms.

(1993) interpreted the unbalanced Ca^{2+} occupancy of the two split crystallographic sites in terms of a dynamical model in which the $I\bar{1}$ phase is a statistical dynamical average of small, mobile $P\bar{1}$ domains. Each of the Ca atoms of the $I\bar{1}$ cell apparently flip unequally between alternate positions violating the symmetry and probably accounting for the persistence of extremely diffuse c reflections.

This work describes the study of calcination products obtained starting from primary raw materials (kaolin, aluminum hydroxide) and a secondary raw material, the product of the thermal transformation of cement-asbestos. The increased need for alternative solutions to disposal in landfills prompts recycling of both hazardous (such as asbestos containing material ACM) and non-hazardous wastes as secondary raw materials for various manufacture processes. Recycling is promoted by the recent European Directive 2008/98/EC of 19-11-2008 and in Italy by the Italian D. Lgs. 152, 03-04-2006 “*Codice ambientale*”. Even if asbestos is banned in Italy since 1992, ACM may still be found in the environment. It is estimated that approximately 2 billion m^2 of cement-asbestos slates still cover roofs of industrial plants and civil buildings (Gualtieri et al., 2009). Since all slates invariably show signs of surface degradation, they should be removed or the physical-chemical degradation may prompt the release of asbestos fibers (Babic, 2006; Dias et al., 2008). An alternative to the removal and disposal of cement-asbestos slates is the thermal treatment, a viable solution in Italy thanks to the law no. 248 (D.M. 19/07/2004) which legitimates the thermal destruction of asbestos containing wastes and the recycling of the product of transformation.

Recently, an industrial process for the thermal destruction of asbestos containing wastes, mainly cement-asbestos, has been developed and patented (Gualtieri et al., 2008). The product of the thermal inertization at 1200 °C is chiefly

composed of SiO_2 and CaO (about 40 wt% each). Having reassured its non-hazardous nature (Giantomassi et al., 2010), the challenge now is to find suitable recycling solutions. Previous works have shown that this secondary raw material can be successfully recycled in the production of construction and building materials such as stoneware tiles (Gualtieri et al., 2008), clay bricks, glasses, glass-ceramics, ceramic frits, ceramic pigments and plastic materials (Gualtieri et al., 2010). As a further step towards full recycling, this secondary raw material could be used as CO_2 -free source of Ca, substituting Ca-carbonates and permitting to reduce the CO_2 emissions during the industrial manufacture processes.

The recycling of the product of the thermal inertization of cement-asbestos at 1200 °C for the synthesis of anorthite is described here. The obtained synthetic anorthite has been fully characterized with SEM and TEM electron microscopy supported by X-ray microanalysis, Rietveld structure refinement and complementary spectroscopic analyses including Mössbauer and UV-Vis.

Experimental

Materials

The secondary raw material used in this study (named KRY•AS) was prepared by prolonged thermal treatment of a standard sealed pack of 61 cement asbestos slates removed from an industrial site and ready to be disposed in controlled landfill. The pack was placed in a discontinuous industrial kiln and subjected to a temperature ramp with a total duration of 40 h, including a 21 h long isothermal step at 1200 °C. The characterization of the untreated slates and KRY•AS, as well as details of the firing cycle are described in Gualtieri et al. (2008). The high temperature transformation of cement-asbestos prompted the formation of cement phases such as C2S and ferrite (ideally $\text{Ca}_4\text{Al}_2\text{Fe}_2\text{O}_{10}$), and

Al-,Ca-,Mg-rich silicates such as akermanite (ideally $\text{Ca}_2\text{MgSi}_2\text{O}_7$) and merwinite (ideally $\text{Ca}_3\text{MgSi}_2\text{O}_8$).

Different sources of commercial natural kaolins were used. The best sample resulted to be a nearly pure kaolinite with impurities of quartz and illite below 10 wt%. Synthetic aluminum hydroxide is provided by Aldrich Chemistry (98.5 wt% purity).

Synthesis conditions

More than 40 experiments were conducted to optimize the synthesis conditions. During the preliminary experimental stage, the following parameters were varied and optimized to accomplish the final synthesis recipe: (i) different sources and relative weight of the raw materials; (ii) addition of mineralizers; (iii) mixing (dry or wet) and milling times (dry or wet); (iiii) maximum temperature, isothermal time and heating/cooling ramp gradients of the calcination curve. For each experiment, the yield of reaction was tested with X-ray qualitative phase analysis.

The formulations were prepared by following the protocol used to reproduce the standard production of ceramic pigments. The mixes were wet milled in a porcelain ball mill for 25 min with alumina balls, 50 mass% water and 0.3-0.5 mass% sodium silicate deflocculant. With this milling procedure, a solid residue of about 1 mass% on the 16000 mesh/cm² (44 mm) sieve was obtained. The powders were placed in alumina crucibles for the calcinations step. The firing curves to reproduce industrial firing cycles accomplished a maximum firing temperature of about 1200-1250 °C. The muffle kiln used for the calcinations is a Lenton UAF17 with a maximum operating temperature of 1700 °C. Out of all the preliminary tests, the most promising formulation was fully characterized. Such formulation was also reproduced in an industrial laboratory using the manufacture conditions.

Characterization of the synthetic anorthite

To verify the yield of reaction, all the products of calcinations were powdered in an agate mortar and investigated by X-ray diffraction. Qualitative phase analysis of each sample was performed using a Philips PW1730 X-ray diffractometer with Ni-filtered Cu K α radiation at 40 kV and 30 mA, 1/2° divergence and receiving slits, and step scan of 0.02° 2 θ . Samples were collected using the side loading technique in the 3-80° 2 θ range. The best formulation of synthetic anorthite was fully characterized with chemical-physical and mineralogical-crystallographic methods.

The chemical analysis of the major and minor elements was performed using X-ray fluorescence (XRF) spectroscopy (Philips PW2480).

⁵⁷Fe-Mössbauer spectra were measured at room temperature, using a conventional spectrometer system operated in constant acceleration mode with a ⁵⁷Co source of nominal strength of 25 mCi in rhodium matrix, and recorded with a multi-channel analyzer using 512 channels. After velocity calibration against a spectrum of high-purity α -iron foil (25 μm thick), the raw data were folded to 256 channels. To have good statistics, about 5 million counts per channel were collected. For each sample about 100 mg were available and Fe total content was between 1 and 5 wt %, so that the absorber was within the limits for the thin absorber thickness described by Long et al. (1983). The velocity range -10 to 10 mm/s was investigated to detect magnetic oxide impurities, in case they were present. The spectrum was fit using the Recoil 1.04 fitting program (Lagarec and Rancourt, 1988). Data analysis involved a curve-fitting procedure made by assuming a Lorentzian peak shape, and the statistical best fit was obtained by using the reduced χ^2 method, with uncertainties estimated on the basis of the covariance matrix. The experimental errors were estimated to be about ± 0.02 mm/s for center shift (CS),

quadrupole splitting (QS) and peak full width at half maximum (FWHM). The doublet areas were measured with uncertainties no less than $\pm 3\%$.

The UV-Vis spectra were collected using a Jasco V-570 spectrophotometer in the 380-780 nm region. The acquisition software of the instrument automatically calculates the colour parameters in the CieLab colour space.

The mineralogical quantitative phase analysis was determined using X-ray powder diffraction and the Rietveld method. The addition of a known amount of internal standard to the sample (fluorite in this case) allowed to achieve a reliable estimate of both the amorphous and crystalline fractions (Gualtieri, 2000).

The XRPD data used for these analyses were collected using a PANalytical θ/θ diffractometer (CuK α radiation, 40 kV and 40 mA), equipped with a real time multiple strip (RTMS) detector. Data were collected in the range 3-80° 2 θ in continuous mode, with a Ni filter on the primary beam, 1/4° fixed divergence slits, 0.0023° soller slit on both the incident and secondary beam, 1/4° fixed antiscatter slit, and fixed 5 mm RTMS slit. An integrated step scan of the RTMS detector of 0.0167273° 2 θ was used with a virtual counting statistics of 25 s/step. The quantitative phase analysis QPA analysis was performed using the GSAS (Larson and Von Dreele, 1999) software and its graphical interface EXPGUI (Toby, 2001).

To follow the calcination dynamics of the best formulation in situ, HTXRD experiments were performed with the same instrument described above. The diffractometer is also equipped with an Anton Paar HTK16 heating chamber (Graz, Austria). The utilization of a fast RTMS10 detector allowed monitoring the phase transformations using the time scale of the in-house calcination experiment. The sample powder was placed upon the Pt strip, which is at the same time thermocouple, heating element, and sample holder. The calibration of temperature was obtained by following the

thermal expansion of standard samples such as Si NIST 640c, pure synthetic periclase, and pure α -alumina (corundum NIST 676). Patterns have been collected in continuous mode in 5-40° 2 θ range, with 40 KV, 40 mA, 1/4° fixed divergence slits, 0.0023° soller slit on both the incident and secondary beam, 1/4° fixed antiscatter slit; fixed 5 mm RTMS slit; and Ni filter on the secondary beam. An integrated step scan of 0.0167273° 2 θ was used and 15 s/step as counting statistics (about 2 min per measurement). Data were collected from 25 to 1200 °C, at steps of 100 °C, with heating/cooling rate to match the calcinations curve.

The Rietveld structure refinement was conducted on powder data collected using the same instrument setting. Data were collected in the range 3-120° 2 θ in continuous mode, with a Ni filter on the primary beam, 1/4° fixed divergence slits, 0.0023° soller slit on both the incident and secondary beam, 1/4° fixed antiscatter slit, and fixed 5 mm RTMS slit. An integrated step scan of the RTMS detector of 0.0167273° 2 θ was used with a virtual counting statistics of 250 s/step. The structure refinements were performed using the GSAS (Larson and Von Dreele, 1999) software and its graphical interface EXPGUI (Toby, 2001).

The starting atomic coordinates in space group $I\bar{1}$ of the final refinement were taken from Angel (1988). Other structure models in $P\bar{1}$ were tested for the refinement but invariably led to unreliable results. The background profile was fitted with a Chebyshev polynomial function with 12 coefficients. The profile of the diffraction peaks was modelled using a pseudo-Voigt function with one Gaussian and two Lorentzian coefficients. The refinement of the atomic coordinates, the atomic site occupancies for extra-framework positions, and the isotropic thermal parameters have been performed with the aid of soft constraints. Soft constraints on the Si-O = 1.60(2) Å and Al-O = 1.74(2) Å were imposed with an initial weight of 10⁶ and used

as additional observations in the earlier stages of the refinement and progressively reduced down to the value of 15.

Powdered samples were investigated with scanning electron microscopy (SEM). The specimens were mounted on Al stubs and coated with gold (10 nm thick film). Micrographs were taken using a Philips XL 40/604 instrument equipped with X-ray microanalysis detector which allows a spot quantitative chemical analysis.

The TEM images and electron diffraction patterns were collected using a JEOL 2010 microscope, working at 200 kV, equipped with LaB6 source and ultra-high resolution (UHR) pole pieces capable of 0.19 nm point resolution. A TV-rate CCD camera with image amplifier was used for focus and astigmatism corrections. Electron images and selected area electron diffraction (SAED) patterns were recorded by photographic films.

Results and Discussion

The best formulation for the synthesis of anorthite is composed of KRY·AS 27.8 wt%, kaolin 42.9 wt%, aluminum hydroxide 26.4 wt%, and boric acid as mineralizer 2.9 wt%. The

calcinations curve used to obtain the best synthetic anorthite sample accomplishes a heating rate of 30 °C, an isothermal step at 1200 °C for 1 h, and a cooling rate of 10 °C down to 25 °C. The result has been reproduced in an industrial laboratory using a discontinuous muffle kiln which permitted to replicate the in-house calcination cycle. The X-ray diffraction study (not reported here) demonstrated the reproducibility of the result even under industrial conditions. The powder sample obtained with the industrial calcination was also used for the spectroscopic characterization.

The XRF analysis of the synthetic powder yielded the following chemical composition: oxides of the major elements (wt%) are SiO₂ = 35.47, Al₂O₃ = 40.99, Fe₂O₃ = 1.32, TiO₂ = 0.31, CaO = 17.96, MgO = 3.46, Na₂O = 0.15, K₂O = 0.31, MnO = 0.03; minor elements (ppm) are Ni = 93, Co = 15, Cr = 78, V = 49, Ce = 24, Nd = 11, Ba = 127, La = 16, Nb = 5, Zr = 131, Y = 6, Sr = 391, Rb = 21, Pb = 23, Zn = 52, Cu = 19, S = 45, Cl = 23.

The Mössbauer study on both the samples synthesized with the in-house kiln and industrial kiln (see the spectra in Figure 2 and calculated parameters in Table 1) revealed the only presence

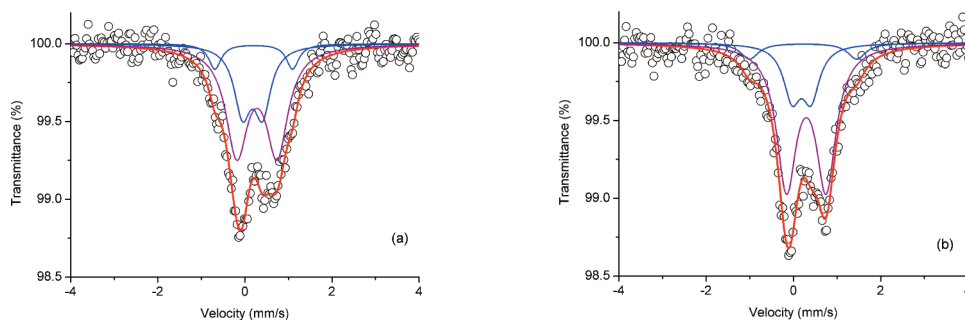


Figure 2. Selected portion (± 4 mm/s) of Mössbauer spectra at room temperature of synthetic calcination products: (a) the sample synthesized in laboratory at 1200 °C; (b) the sample synthesized with the industrial process. Black circles = experimental spectrum; red line = calculated spectrum; blue line = contribution of tetrahedrally-coordinated Fe³⁺; purple line = contribution of octahedrally-coordinated Fe³⁺.

Table 1. Room temperature Mössbauer parameters of synthetic calcination products.

| Sample | Temperature | CS [mm/s] | QS [mm/s] | FWHM [mm/s] | Intensity [%] | Attribution |
|--------------------|-------------|--------------|--------------|----------------|------------------|------------------------|
| Lab sample 1200 | 294 K | 0.18 | 0.46 | 0.46 | 29 | Tetr. Fe ³⁺ |
| | | 0.20 | 1.78 | 0.34 | 8 | Tetr. Fe ³⁺ |
| | | 0.28 | 0.93 | 0.60 | 63 | Oct. Fe ³⁺ |
| Industrial sample | 294 K | 0.19 | 0.43 | 0.48 | 22 | Tetr. Fe ³⁺ |
| | | 0.22 | 2.46 | 0.50 | 8 | Tetr. Fe ³⁺ |
| | | 0.30 | 0.91 | 0.54 | 70 | Oct. Fe ³⁺ |

Note: CS: centre shift (with respect to α -iron); QS: quadrupole splitting; FWHM: full width at half maximum. Estimated uncertainties (2σ) are about 0.02 mm/s for CS, QS, FWHM, and no less than 3% for intensity. Tetr. Fe³⁺ = Tetrahedrally coordinated Fe³⁺; Oct. Fe³⁺ = Octahedrally coordinated Fe³⁺.

of Fe³⁺, and pointed to a distribution of this Fe³⁺ in tetrahedral (about 1/3) and octahedral (about 2/3) environments. No evidence of magnetic Fe-oxides (e.g., hematite, maghemite etc.) was observed. The presence of tetrahedrally-coordinated Fe³⁺ is not surprising because thermally treated cement-asbestos used as precursor of the present anorthite synthesis already contained tetrahedrally-coordinated Fe³⁺. In fact, Giacobbe et al. (2010) found that the high

intensity of the pre-edge iron-XANES peak of the high temperature product of cement-asbestos was comparable with that of the reference compound Fe-silicalite, a zeolite containing iron in the framework tetrahedral sites.

The UV-Vis spectrum of the final product of the calcination is reported in Figure 3: a smeared band is observed at about 469 nm. This band is considered to be diagnostic for structural Fe³⁺ (Burns, 1993). Anyway, the strongest absorption is in the UV region (below 400 nm), and the observed absorption in the Vis region is rather weak in intensity. This is reflected also by the measured CieLab color parameter L (indicative of the whiteness of the powder), which is around 91 out of 100 in the present case.

The HT in situ dynamics of the calcination process shows the following major reaction steps: Al(OH)₃ decomposes between 300 and 400 °C, kaolinite decomposes between 450 and 600 °C leaving a broaden band around 20° 2 θ typical of metakaolinite (Gualtieri and Bellotto, 1998), secondary calcite decomposes between

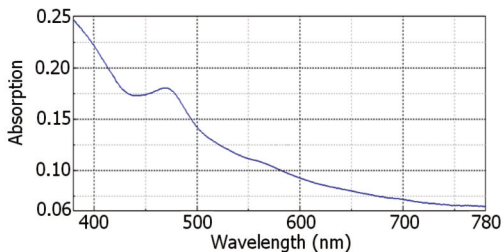


Figure 3. The UV-Vis pattern of synthetic calcination products in the 380-780 nm range.

650 and 800 °C and prompts the formation of CaO, quartz is not stable above 1000 °C in correspondence with the crystallization of anorthite. The reaction of crystallization of anorthite is accomplished during the isothermal step at 1200 °C.

The Rietveld quantitative phase analysis with the internal standard revealed that the best formulation of synthetic anorthite obtained with the synthesis route described above is actually a multiphase system with anorthite 88.9(1) wt% and spinel 11.1(1) wt%. The structure model of spinel *sensu stricto* (s.s.) was taken from Redfern et al. (1999) with a starting unit cell parameter of 8.0836 Å, and the refined unit cell of 8.1019(2) Å was obtained.

The presence of Fe³⁺ revealed by XRF, Mössbauer and UV-Vis raises the question if this transition element is hosted either by anorthite or by spinel. The first hypothesis would be quite unusual and should not be favored by steric as well as energetic considerations. On the contrary, it is well known that spinel structure may easily host Fe³⁺, which substitutes for Al in the MgAl₂O₄ - MgFe₂O₄ spinel s.s. - magnesioferrite series (Andreozzi et al., 2001a; 2001b). In the previous studies it was observed that the effect of incorporation of fairly small quantities of Fe³⁺ in synthetic spinel s.s. is the regular increase of cell parameter (up to 8.1174 Å for Fe₂O₃ contents of approximately 11 wt%). This is very relevant to the present case, because if all Fe₂O₃ was confined in the spinel phase, this would explain the relatively high value of spinel cell parameter here refined. Moreover, it was observed by Andreozzi et al. (2001a) that some tetrahedrally-coordinated Fe³⁺ is normally present in a disordered, synthetic spinel produced at high temperature. The electronic transitions due to interactions between tetrahedrally- and octahedrally-coordinated Fe³⁺ in spinel were shown by previous authors to determine UV-Vis absorption at 21300 cm⁻¹, that is 469 nm, in perfect agreement to what recorded here.

In spite of this, direct evidences were sought after. SEM images of the synthetic anorthite disclose beautiful well formed crystals with an average size of ca. 5 µm (Figure 4). More than 50 microanalyses were conducted on different specimens in the attempt to further verify if iron is associated with the anorthite crystals or not. EDS analytical maps were also collected to evidence the element distribution in the samples. The clear outcome of the tests is that iron is never associated with a crystalline or even microcrystalline phase with a chemical composition compatible with that of anorthite (Figure 5a), but it is invariably associated with a crystalline phase chemically compatible with spinel (Figure 5b). In particular, the spinel-like phase is quite similar in morphology to poor-quality, synthetic spinel crystals obtained by Quintiliani et al. (2011) when inappropriate experimental conditions were used. In conclusion, there are many convincing evidences that iron is hosted in the structure of spinel and that the existence of a Fe-anorthite synthetic product should be ruled out.

The TEM study revealed that a number of anorthite crystals are actually twins (Figure 6a). The electron diffraction pattern, besides the

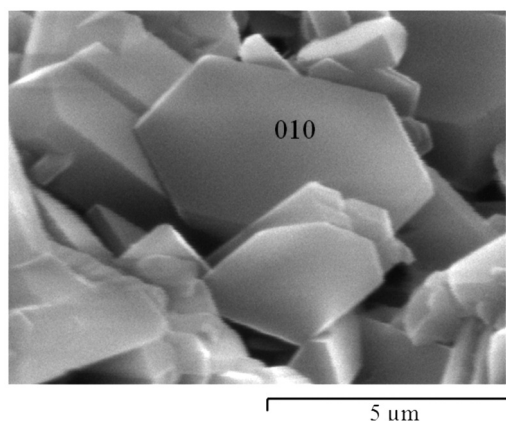


Figure 4. Selected SEM image of synthetic anorthite crystals. Indication of the crystal face (010) is also reported for clarity.

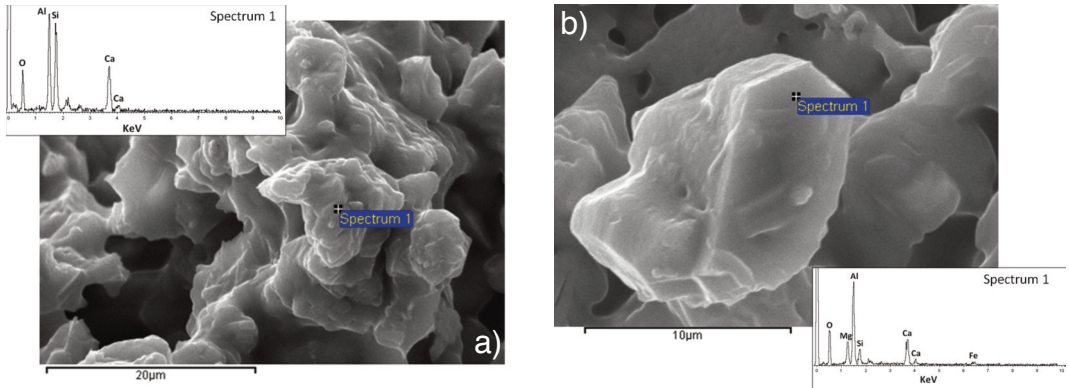


Figure 5. Secondary electrons image and spot chemical analysis of synthetic calcination products: (a) an anorthite rich area showing the absence of the iron peak; (b) a spinel rich area showing the presence of the iron peak.

reflection satellites, evidenced extra reflections along the c axis typical of P -anorthite (Figure 6b). It is known that anorthite cooled below 250 °C shows long-range order of the Ca atoms and that collapse of the framework around them drops the real symmetry to $P\bar{1}$. Complex domain textures develop with each domain showing long-range order in which the Ca atoms are displaced. The smaller the domains, the more diffuse are the ‘ c ’ diffractions which characterize P -anorthite (Yund, 1983). Notwithstanding, as already reported by Angel (1988), owing to the

large number of parameters and low numbers of observed reflections, correlation problems develop in the refinement of a structure with primitive symmetry. Therefore, the refinement of our sample was conducted in $I\bar{1}$. In a future work it would be interesting to collect low temperature neutron diffraction data in the attempt to refine the structure in $P\bar{1}$.

The Rietveld structure refinement was conducted in space group $I\bar{1}$. Graphical result of the Rietveld refinement (observed vs. calculated curve and difference curve) is shown in Figure

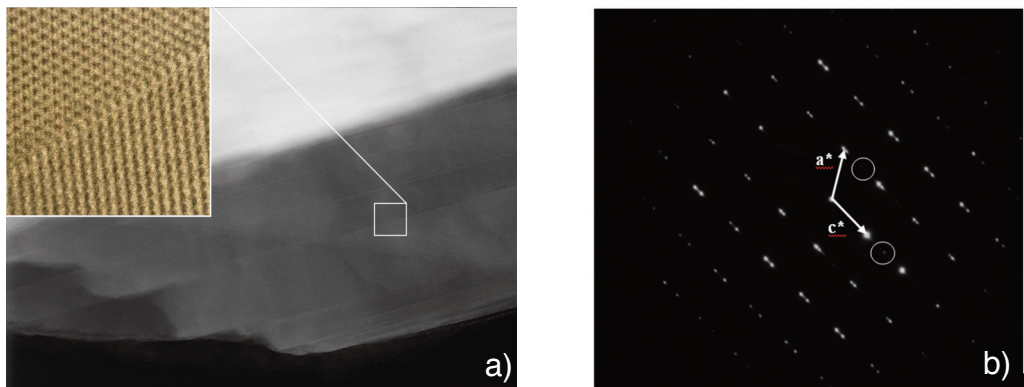


Figure 6. Twinned synthetic anorthite crystals: (a) TEM image; (b) relative SAED electron diffraction pattern of the a^* - c^* plane.

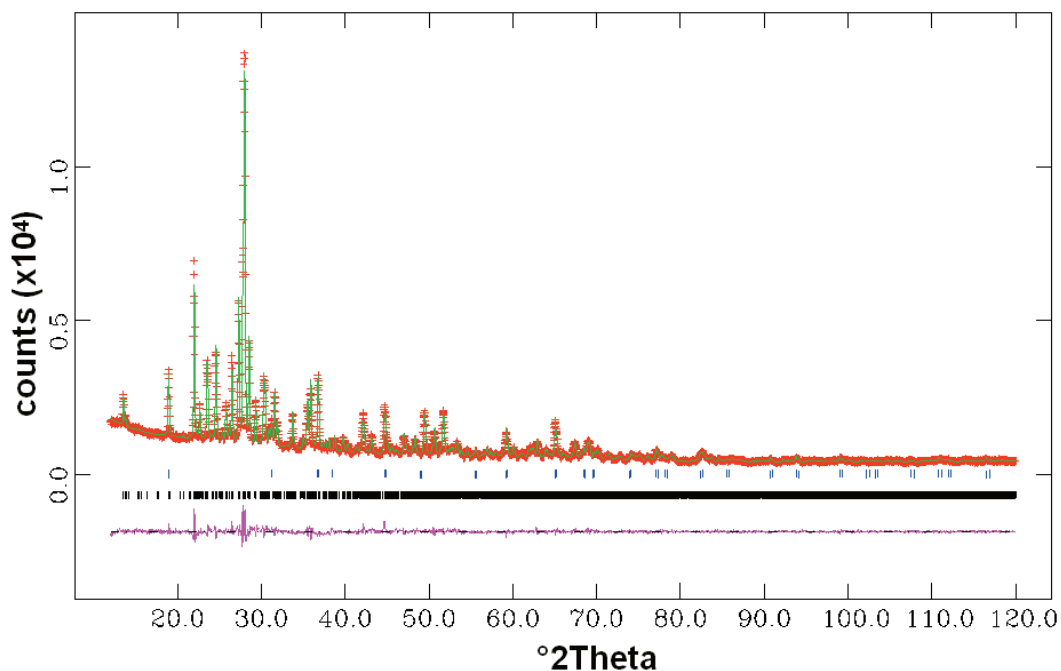


Figure 7. The observed vs. calculated curve and difference curve of the Rietveld refinement of synthetic anorthite. Reflections legend: first row from the bottom = anorthite; second row from the bottom = spinel.

7. The agreement factors are: $R_{wp} = 4.89\%$, $R_p = 3.76\%$, $\chi^2 = 2.141$, $R(F^2) = 6.31\%$. The raw data and GSAS experimental file of the refinement are available upon request to the author. The calculated unit cell is $a = 8.1808(2) \text{ \AA}$, $b = 12.8729(3) \text{ \AA}$, $c = 14.1621(3) \text{ \AA}$, $\alpha = 93.137(2)^\circ$, $\beta = 115.708(1)^\circ$, $\gamma = 91.246(2)^\circ$.

Structural parameters of synthetic anorthite are reported in Table 2, and interatomic distances of the framework and extra-framework atoms in Tables 3 and 4.

Likewise the structure reported by Angel (1988) the Ca atoms are disordered over four sites with a 50% population. Ca_{000} and Ca_{z00} display a 6-fold coordination with oxygen atoms at an average distance of 2.524 and 2.457 \AA , respectively. Ca_{010} and Ca_{z10} show a distorted 7-fold coordination with the oxygen atoms at an average distance of 2.522 and 2.575 \AA ,

respectively (Table 4). The average Ca-O distances are in very good agreement with those reported by Angel (1988), the only difference being the Ca_{010} atom which displays a 7-fold coordination environment.

Concluding remarks

In this paper, the synthesis route of anorthite and its full characterization are described. The highest yield of reaction was obtained by calcination at 1200 $^\circ\text{C}$ for 1 h of a mix composed of a secondary raw material (the thermal transformation of cement-asbestos) kaolin, aluminum hydroxide, and boric acid as mineralizing agent.

The Rietveld structure refinement was performed in space group $I \bar{1}$ on the powder sample representative of the optimal synthesis

Table 2. Structural parameters of synthetic anorthite.

| Site | x/a | y/b | z/c | Chemical species | Site population | $U_{iso}(\text{\AA}^2)$ |
|-------|-----------|-----------|-----------|------------------|-----------------|-------------------------|
| Si1oo | 0.002(2) | 0.1597(8) | 0.107(1) | Si | 1 | 0.011(4) |
| Al1oz | 0.005(2) | 0.1590(9) | 0.6102(9) | Al | 1 | 0.008(3) |
| Al1mo | 0.013(1) | 0.8150(8) | 0.1130(9) | Al | 1 | 0.016(6) |
| Si1mz | -0.002(1) | 0.8162(8) | 0.6161(9) | Si | 1 | 0.018(3) |
| Al2oo | 0.688(1) | 0.1200(8) | 0.1619(8) | Al | 1 | 0.009(3) |
| Si2oz | 0.674(1) | 0.0962(7) | 0.6536(8) | Si | 1 | 0.013(3) |
| Si2mo | 0.675(1) | 0.8825(8) | 0.1747(9) | Si | 1 | 0.013(4) |
| Al2mz | 0.683(2) | 0.8718(8) | 0.6828(9) | Al | 1 | 0.007(4) |
| Caooo | 0.722(2) | 0.979(1) | 0.079(1) | Ca | 0.5 | 0.021(7) |
| Cazoo | 0.282(4) | 0.038(2) | 0.550(2) | Ca | 0.5 | 0.021(7) |
| Caoio | 0.778(3) | 0.542(1) | 0.543(1) | Ca | 0.5 | 0.021(7) |
| Cazio | 0.747(2) | 0.509(1) | 0.067(2) | Ca | 0.5 | 0.021(7) |
| Oa1o | 0.000(3) | 0.118(1) | -0.004(1) | O | 1 | 0.008(6) |
| Oa1z | 0.010(3) | 0.131(1) | 0.487(1) | O | 1 | 0.018(7) |
| Oa2o | 0.591(2) | 0.9951(8) | 0.144(2) | O | 1 | 0.015(6) |
| Oa2z | 0.572(2) | 0.9957(9) | 0.640(2) | O | 1 | 0.029(7) |
| Oboo | 0.826(2) | 0.095(1) | 0.099(1) | O | 1 | 0.010(6) |
| Oboz | 0.789(2) | 0.109(1) | 0.585(1) | O | 1 | 0.014(7) |
| Obmo | 0.828(2) | 0.859(1) | 0.132(2) | O | 1 | 0.018(6) |
| Obmz | 0.812(2) | 0.855(1) | 0.612(1) | O | 1 | 0.006(6) |
| Ocoo | 0.003(2) | 0.2823(9) | 0.134(2) | O | 1 | 0.006(8) |
| Ocoz | 0.025(2) | 0.291(1) | 0.645(2) | O | 1 | 0.007(7) |
| Ocmo | 0.015(2) | 0.6777(9) | 0.112(2) | O | 1 | 0.007(9) |
| Ocmz | -0.002(2) | 0.691(1) | 0.599(2) | O | 1 | 0.019(7) |
| Odoo | 0.1937(2) | 0.114(1) | 0.181(1) | O | 1 | 0.025(7) |
| Odoz | 0.196(2) | 0.097(1) | 0.699(1) | O | 1 | 0.012(7) |
| Odmo | 0.197(2) | 0.869(1) | 0.2241(9) | O | 1 | 0.038(5) |
| Odmz | 0.186(2) | 0.867(1) | 0.7027(9) | O | 1 | 0.007(5) |

Table 3. Calculated tetrahedral interatomic distances involving Si and Al.

| Distance | Value (Å) | Distance | Value (Å) |
|--------------|-----------|--------------|-----------|
| Si1oo-Oa1o | 1.629(7) | Al1oz-Oa1z | 1.773(8) |
| Si1oo-Oboo | 1.603(6) | Al1oz-Oboz | 1.740(7) |
| Si1oo-Ocoo | 1.605(7) | Al1oz-Ocoz | 1.732(8) |
| Si1oo-Odoo | 1.607(7) | Al1oz-Odoz | 1.765(7) |
| mean Si1oo-O | 1.611 | mean Al1oz-O | 1.752 |
| Si1mz-Oa1z | 1.627(7) | Al1mo-Oa1o | 1.768(7) |
| Si1mz-Obmz | 1.597(7) | Al1mo-Obmo | 1.752(7) |
| Si1mz-Ocmz | 1.619(7) | Al1mo-Ocmo | 1.767(7) |
| Si1mz-Odmz | 1.590(7) | Al1mo-Odmo | 1.733(7) |
| mean Si1mz-O | 1.608 | mean Al1mo-O | 1.755 |
| Si2oz-Oa2z | 1.594(7) | Al2oo-Oa2o | 1.732(8) |
| Si2oz-Oboz | 1.631(7) | Al2oo-Oboo | 1.751(7) |
| Si2oz-Ocmo | 1.614(6) | Al2oo-Ocmz | 1.725(7) |
| Si2oz-Odmo | 1.618(7) | Al2oo-Odmz | 1.735(6) |
| mean Si2oz-O | 1.614 | mean Al2oo-O | 1.736 |
| Si2mo-Oa2o | 1.618(6) | Al2mz-Oa2z | 1.738(8) |
| Si2mo-Obmo | 1.634(7) | Al2mz-Obmz | 1.745(7) |
| Si2mo-Ocoz | 1.580(7) | Al2mz-Ocoo | 1.716(7) |
| Si2mo-Odoz | 1.637(7) | Al2mz-Odoo | 1.744(7) |
| mean Si2mo-O | 1.617 | mean Al2mz-O | 1.736 |

Table 4. Calculated interatomic distances involving atoms the Ca atoms.

| Distance | Value (Å) | Distance | Value (Å) |
|--------------|-----------|--------------|-----------|
| Ca000-Caoio | 0.999(19) | Caoio-Oa1o | 2.329(27) |
| Ca000-Oa1o | 2.772(24) | Caoio-Oa1o | 2.881(28) |
| Ca000-Oa1o | 2.308(26) | Caoio-Oa2o | 2.439(25) |
| Ca000-Oa2o | 2.360(21) | Caoio-Oboo | 2.425(25) |
| Ca000-Oboo | 2.419(23) | Caoio-Obmo | 2.647(26) |
| Ca000-Odoo | 2.471(23) | Caoio-Ocmz | 2.448(24) |
| Ca000-Odmo | 2.817(24) | Caoio-Odoo | 2.486(27) |
| Mean Ca000-O | 2.524 | Mean Caoio-O | 2.522 |
| Cazoo-Cazio | 0.575(27) | Cazio-Oa1z | 2.426(29) |
| Cazoo-Oa1z | 2.383(32) | Cazio-Oa1z | 2.564(27) |
| Cazoo-Oa2z | 2.294(29) | Cazio-Oa2z | 2.437(25) |
| Cazoo-Oboz | 2.487(30) | Cazio-Oboz | 2.471(27) |
| Cazoo-Obmz | 2.578(27) | Cazio-Ocmo | 2.889(23) |
| Cazoo-Ocmo | 2.426(26) | Cazio-Odoz | 2.327(26) |
| Cazoo-Odoz | 2.573(30) | Cazio-Odmz | 2.911(21) |
| Mean Cazoo-O | 2.457 | Mean Cazio-O | 2.575 |

conditions and about 90 wt% of anorthite was found. The remaining 10 wt% is made of spinel s.s., which incorporated the fairly low amounts of Fe present in the thermally treated cement-asbestos used as precursor of the present anorthite synthesis.

Color of the synthetic product is fairly white due to the absence of iron oxides (such as hematite or maghemite), and this suggests its possible utilization as white pigment for traditional ceramics. To this aim, new experiments at industrial scale should be conducted to verify the stability of synthetic anorthite in stoneware tile body mixes. In addition, the highly expensive aluminum hydroxide which was utilized for the formulation

of synthetic anorthite could be substituted with other cheap primary raw materials or Al-rich secondary raw materials, to make this product more competitive on the market.

Acknowledgements

Part of this paper is the outcome of the degree thesis of L. Sardisco. The assistance of P. Bertocchi (Ferro Italian branch, Fiorano modenese, Italy) for the industrial synthesis is acknowledged. The two referees G. Cruciani and D. Levy are warmly acknowledged for their careful revision which prompted a thorough reinterpretation of the experimental results and a substantial revision of the original structure models.

References

- Andreozzi G.B., Halenius U. and Skogby H. (2001a) - Spectroscopic active $^{IV}Fe^{3+}$ - $^{VI}Fe^{3+}$ clusters in spinel-magnesian ferrite solid solution crystals: a potential monitor for ordering in oxide spinels. *Physics and Chemistry of Minerals*, 28, 435-444.
- Andreozzi G.B., Lucchesi S., Skogby H. and Della Giusta A. (2001b) - Composition dependence of cation distribution in some synthetic (Mg, Zn) (Al, Fe^{3+})₂O₄ spinels. *European Journal of Mineralogy*, 13, 391-402.
- Angel R.J. (1988) - High-pressure structure of anorthite. *American Mineralogist*, 73, 1114-1119.
- Angel R.J. Carpenter M.A. and Finger L.W. (1990) - Structural variation associated with compositional variation and order-disorder behaviour in anorthite-rich feldspars. *American Mineralogist*, 75, 150-162.
- Babic B.R. (2006) - The use of cement fibre composites in prolonged wet environments. In: 10th International Inorganic-Bonded Fiber Composites Conference, Curran Associates, São Paulo, 260-273.
- Burns R. G. (1993) - Mineralogical Application of Crystal Field Theory. Cambridge University Press pp. 551.
- Carpenter M.A. (1991) - Mechanisms and kinetics of Al-Si ordering in anorthite. I, Incommensurate structure and domain coarsening. *American Mineralogist*, 76, 1110-1119.
- Dias C.M.R., Cincotto M.A., Savastano H. Jr and John V.M. (2008) - Long-term aging of fiber-cement corrugated sheets. The effect of carbonation, leaching and acid rain. *Cement and Concrete Composites*, 30, 255-265.
- Faye G.H. (1969) - The optical absorption spectrum of tetrahedrally bonded Fe^{3+} in orthoclase. *Canadian Mineralogist*, 10, 112-118.
- Ghose R.K., McMullan, H.P. and Weber H.P. (1993) - Neutron diffraction studies of the $P\bar{1}$ - $I\bar{1}$ transition in anorthite, CaAl₂Si₂O₈, and the crystal structure of the body-centered phase at 514K. *Zeitschrift für Kristallographie*, 204, 215-237.
- Giacobbe C., Gualtieri A. F., Quartieri S., Rinaudo C., Allegrina M. and Andreozzi G.B. (2010) - Spectroscopic study of the product of thermal transformation of chrysotile-asbestos containing materials (ACM). *European Journal of Mineralogy*, 22, 535-546.
- Giantomassi F., Gualtieri A.F., Santarelli L., Tomasetti M., Lusvardi G., Lucarini C., Governa M. and Pugnali A. (2010) - Biological effects and comparative cytotoxicity of thermal transformed asbestos-containing materials in a human alveolar epithelial cell line. *Toxicology in vitro*, 24, 1521-1531.
- Gualtieri A.F. (2000) - Accuracy of XRPD QPA using the combined Rietveld-RIR method. *Journal of Applied Crystallography*, 33, 267-278.
- Gualtieri A.F. and Bellotto M. (1998) - Modelling the structure of the metastable phases in the reaction sequence kaolinite-mullite by X-ray scattering experiments. *Physics and Chemistry of Minerals*, 25, 442-452.
- Gualtieri A. F., Cavenati C., Zanatto I., Meloni M., Elmi G. and Lassinantti Gualtieri M. (2008) - The transformation sequence of cement-asbestos slates up to 1200 °C and safe recycling of the reaction product in stoneware tile mixtures. *Journal of Hazardous Materials*, 152, 563-570.
- Gualtieri A.F., Mangano D., Lassinantti Gualtieri M., Ricchi A., Foresti E., Lesci G., Roveri N., Mariotti M. and Pecchini G. (2009) - Ambient monitoring of asbestos in selected Italian living areas. *Journal of Environmental Management*, 90, 3540-3552.
- Gualtieri A. F., Giacobbe C., Sardisco L., Saraceno M., Lassinantti Gualtieri M., Lusvardi G., Cavenati C. and Zanatto I. (2010) - Recycling of the product of thermal inertization of cement-asbestos for various industrial applications. *Waste Management*, 31, 91-100.
- Iiischi K., Tomisaka T., Kato T., Yimaguchi and Umegaki Y. (1971) - Isomorphous substitution and infrared and far infrared spectra of the feldspar group. *Neues Jahrbuch für Mineralogie Abhandlungen*, 115, 98-119.
- Lagarec K. and Rancourt D.G. (1997) - Extended Voigt-based analytic lineshape method for determining N-dimensional correlated hyperfine parameter distributions in Mössbauer spectroscopy. *Nuclear Instruments and Methods in Physics Research Section B: Beam Interactions with Materials and Atoms*, 129, 266-280.
- Larson A.C. and Von Dreele R.B. (2000) - General Structure Analysis System (GSAS). Los Alamos National Laboratory Report (LAUR 86-748), Los Alamos, New Mexico, 224 pp.
- Long G.J., Cranshaw T.E. and Longworth G. (1983) - The ideal Mössbauer effect absorber thickness.

- Mössbauer Effect Reference and Data Journal*, 6, 42-49.
- Phillips M.W. Kirkpatrick R. J. and Carpenter M.A. (1992) - Investigation of short-range Al, Si order in synthetic anorthite by Si MAS NMR spectroscopy. *American Mineralogist*, 77, 484-494.
- Quintiliani M., Andreozzi G.B. and Skogby H. (2011) - Synthesis and Mössbauer characterization of $\text{Fe}_{1+x}\text{Cr}_{2-x}\text{O}_4$ ($0 \leq x \leq 2/3$) spinel single crystals. *Periodico di Mineralogia*, 80, 39-55.
- Redfern S.A.T., Harrison R.J., O'Neill H.St.C. and Wood D.R.R. (1999) - Thermodynamics and kinetics of cation ordering in MgAl_2O_4 spinel up to 1600 °C from in situ neutron diffraction. *American Mineralogist*, 84, 299-310.
- Ribbe P.H. (1983) - Chemistry, structure and nomenclature of feldspar. In: Feldspar mineralogy. Reviews in Mineralogy, Ribbe P.H. Editor, Mineralogical Society of America 2, 1-20.
- Salje E.K.H. (1993) - Phase transitions and vibrational spectroscopy in feldspars. In: Feldspars and their reactions. Ed. Parsons., 650 pp.
- Thompson C.S. and Wadsworth M.E. (1957) - Determination of the composition of plagioclase feldspar by means of infrared spectroscopy. *American Mineralogist*, 42, 336-341.
- Toby B.H. (2001) - EXPGUI, a graphical user interface for GSAS. *Journal of Applied Crystallography*, 34, 210-213.
- Wanvik J.E. (2000) - Norwegian anorthosites and their industrial uses, with emphasis on the massifs of the Inner Sogn-Voss area in western Norway. *Ngu-Bull* 436, 103-112.
- Warrel J. (2003) - Properties of the Hermean regolith: III. Disk-resolved vis-NIR reflectance spectra and implications for the abundance of iron. *Icarus*, 161, 199-222.
- Wechsel B.A., Lindsley D.H. and Prewitt C.T. (1984) - Crystal structure and cation distribution in titanomagnetites ($\text{Fe}_{3-x}\text{Ti}_x\text{O}_4$). *American Mineralogist*, 69, 754-770.
- Yund R.A. (1983) - Subsolidus phase relations in the alkali feldspars. In: Feldspar Mineralogy. Reviews in Mineralogy, Ribbe P.H. Editor, Mineralogical Society of America 2, 203-222.

Submitted, August 2010 - Accepted, March 2011

